Thermal design optimization of a parabolic trough collector receiver with a tube-bundle cavity

Original
Thermal design optimization of a parabolic trough collector receiver with a tube-bundle cavity / Ebadi, H., Alarcón-Padilla, D., Guedez, R., Mahmoudi, H., Trevisan, S., Valenzuela, L., Savoldi, L.. - In: SOLAR ENERGY. - ISSN 0038-092X. - 309:(2026). [10.1016/j.solener.2026.114439]

Availability:
This version is available at: 11583/3007961 since: 2026-02-24T08:35:09Z

Publisher:
Elsevier

Published
DOI:10.1016/j.solener.2026.114439

Solar Energy 309 (2026) 114439

Contents lists available at ScienceDirect

Solar Energy

journal homepage: www.elsevier.com/locate/solener

Thermal design optimization of a parabolic trough collector receiver with a tube-bundle cavity

Hossein Ebadi [a,*], Diego-César Alarcón-Padilla [b], Rafael Guedez [c], Hoda Mahmoudi [d], Silvia Trevisan [c], Loreto Valenzuela [b], Laura Savoldi [a]

[a] *MAHTEP Group, Dipartimento Energia "Galileo Ferraris", Politecnico di Torino, Italy*
[b] *Plataforma Solar de Almería, CIEMAT, Spain*
[c] *Energy Department, KTH Royal Institute of Technology, Sweden*
[d] *Absolicon Solar Collector AB, Sweden*

ARTICLE INFO

Keywords:
Concentrated solar power
Parabolic trough collector
Tube-bundle cavity receiver
CFD
Thermo-hydraulic optimization

ABSTRACT

This work presents a numerical investigation of the thermo-hydraulic performance of a tube-bundle cavity (TB) receiver for parabolic trough collectors (PTCs). The proposed receiver replaces the conventional single absorber tube with multiple smaller tubes arranged in a circular bundle, forming a linear cavity that improves solar absorption and reduces temperature non-uniformities on the absorber surface. A three-dimensional CFD model is developed under real-scale operating conditions to assess several TB configurations through a two-stage optimization procedure. The designs are evaluated using thermal efficiency, pressure drop, and overall efficiency metrics. The results indicate that, despite higher flow resistance, TB receivers significantly enhance thermal performance compared to the conventional design. Hotspot temperature increases are reduced by up to 77%, while temperature uniformity increases by approximately 23%. Among the investigated configurations, the 12-tube design provides the best thermo-hydraulic compromise, achieving a maximum overall efficiency of 0.76 at an inlet temperature of 450 K, corresponding to a 7% improvement over the standard receiver. Additional analyses over inlet temperatures ranging from 400 to 550 K confirm the robustness of the optimized TB configuration in mitigating hotspot formation while maintaining superior overall performance.

1. Introduction

Solar energy is expected to play a major role in the future energy mix, with a projected contribution of approximately 25% to global final energy consumption by 2050 [1]. Among solar technologies, concentrated solar thermal (CST) systems are increasingly contributing to renewable electricity and heat generation, supporting the clean energy transition. CST is an indirect energy conversion technology that uses a heat transfer medium to collect, transfer, and store solar thermal energy, enabling applications such as electricity generation, industrial processes, and thermal systems [2]. CST technologies are generally classified into linear and point-focusing systems, characterized by longitudinally uniform and Gaussian-type solar flux distributions, respectively [3]. By the end of 2024, the global installed capacity of CST reached nearly 8 GW [4]. The most widely deployed CST configurations include solar power towers (SPT), parabolic trough collectors (PTC), and linear Fresnel reflectors (LFR), with PTC systems representing the dominant technology in terms of installed capacity [5,6].

As PTC represents the most widely deployed CST technology, accounting for approximately 75% of the installed capacity [7], extensive research efforts have focused on improving their performance. Most thermal enhancement strategies rely on turbulator inserts [8], nanofluids [9], or geometry modifications of the absorber tube [10]. However, these approaches often increase flow resistance, resulting in higher pumping power requirements and increased system costs. Beyond thermal enhancement, improving optical efficiency represents another key factor for enhancing PTC performance and is typically achieved by modifying the strategies for reflecting or absorbing solar energy. One important research direction in this context involves the adoption of cavity receivers in linear solar concentrators [11]. Cavity receivers are inspired by the blackbody principle, whereby an ideal cavity absorbs all incoming radiation independently of the angle of incidence or wavelength [12]. In linear systems, cavity configurations enhance the capture of reflected solar radiation while reducing radiative losses to the surroundings [11]. In PTC applications, cavity concepts are typically

---

* Corresponding author.
E-mail address: hossein.ebadi@polito.it (H. Ebadi).

https://doi.org/10.1016/j.solener.2026.114439
Received 27 October 2025; Received in revised form 28 January 2026; Accepted 15 February 2026

Nomenclature

Abbreviations

BT	Bundle Tube
CFD	Computational Fluid Dynamic
CST	Concentrating Solar Thermal
HTF	Heat Transfer Fluid
IAM	Incidence Angle Modifier
LCR	Local Concentration Ratio
PSA	Plataforma Solar de Almeria
PTC	Parabolic Trough Collector
SCA	Solar Collector Assembly
Std.	Standard pipe
TB	Tube Bundle cavity

Greek symbols

α	absorptance (–)
τ	transmitance (–)
Δp	pressure drop (Pa)
Φ_{in}	incidence angle (rad or degrees)
η	efficiency (–)
ϵ	emittance
ε	turbulent dissipation rate
θ_c	Cavity opening angle (rad or degrees)
κ	turbulent kinetic energy (m^2/s^2)
μ	dynamic viscosity (Pa.s)
ρ	fluid density (kg/m^3)
ρ_r	Parabola specular reflectance (–)
σ	Stefan–Boltzmann constant ($5.67037 \cdot 10^{-8}$ $W/(m^2K^4)$)

Symbols

A	area (m^2)
Cp	specific heat capacity (J/kg/K)
D	diameter (m)
DNI	Direct normal irradiance (W/m^2)
E	heat flux (W/m^2)
f	friction factor (–)
foc	focal length (m)
h	heat transfer coefficient ($W/m^2/K$)
k	thermal conductivity (W/m/K)
L	length (m)
m	mass flow rate (kg/s)
N	cell number
Nu	Nusselt number (–)
p	pressure (Pa)
Q	thermal energy (J)
r	Radius (m)
Re	Reynolds number (–)
T	temperature (K)
V	total volume of the model (m^3)
v	velocity magnitude (m/s)
W	appreture width (m)
W_p	pumping power (W)

Subscripts

amb	ambient
abs	absorbed
cavity	cavity
con	concentrated
conv	convection
en	energy
el	electrical
f	fluid
go	glass outer side
i	inlet
loss	loss
o	outlet
opt	optical
ovr	overall
p	pipe
pi	pipe internal side
po	pipe outer side
rad	radiation
S	solar
sky	sky
th	thermal
u	useful
w	wind
wall	tube wall

implemented either by incorporating a secondary reflector to form a cavity [13], or by redesigning the receiver geometry itself as a cavity absorber [14].

Early investigations on linear cavity absorbers date back to the work of Boyd et al. [15], who demonstrated that shaping the receiver geometry can effectively reduce thermal losses. Subsequent experimental and numerical studies have explored a wide range of cavity-based receiver concepts for parabolic trough collectors. Franceschi [16] reported the application of cavity receivers in an industrial PTC system, while Bader et al. [17] introduced a tubular cavity receiver using air as the heat transfer fluid and internal V-corrugations to enhance heat transfer. More recent numerical investigations have focused on optimizing cavity geometries to improve thermal performance. Liang et al. [18] proposed a linear cavity receiver with inclined fins, achieving a thermal efficiency of 64%, comparable to evacuated tube receivers. Li et al. [14] showed that arc-shaped cavity receivers are particularly suitable for high-temperature operation due to reduced heat losses. Sharifzadeh et al. [19] analyzed a vacuum V-shaped cavity receiver and reported thermal efficiencies up to 72% using coupled optical–thermal models. Further studies have examined the influence of cavity shape and geometric parameters on system performance. Loni et al. [20,21] investigated various cavity configurations and optimized their dimensions, reporting thermal efficiencies up to 82% under specific operating conditions. Experimental validation was provided by Xiao et al. [22], who demonstrated that fin-enhanced V-cavity absorbers significantly improve heat transfer while reducing thermal losses.

Despite the promising thermal and optical performance demonstrated by linear cavity receivers, several challenges still limit their large-scale adoption in parabolic trough collector systems. Many cavity-based designs require substantial modifications to the conventional receiver geometry, often eliminating the evacuated glass envelope or introducing complex sealing solutions, which complicate integration with existing PTC infrastructure. In addition, while numerous studies have reported improved thermal efficiencies, the associated thermo-hydraulic trade-offs have not been systematically addressed. In particular, the impact of cavity configurations on flow distribution, pressure losses, and overall system efficiency under real-scale operating conditions remains insufficiently quantified. Moreover, hotspot mitigation and temperature uniformity, which are critical factors for receiver reliability and lifetime, are often discussed qualitatively rather than through comprehensive thermo-hydraulic analyses. As a result, there is a need for receiver concepts that combine the optical advantages of cavity configurations with full compatibility with conventional evacuated tubular receivers, while providing a balanced assessment of thermal enhancement and hydraulic penalties.

Although many linear cavity receiver concepts aim to eliminate the glass envelope to simplify the system, experimental evidence has shown that the presence of a glass cover can significantly improve thermal performance by reducing convective and radiative losses [23]. However, modifying cavity geometries while maintaining compatibility with standard evacuated tubular receivers remains a major challenge, particularly due to the complexity of vacuum sealing when conventional cylindrical glazing components are used. To address this limitation, Ebadi et al. [24] proposed a novel parabolic trough receiver concept based on a circular arrangement of multiple absorber tubes distributed along the same circumference as a conventional single tube. This configuration simultaneously integrates tube-bundle and cavity concepts, enabling seamless compatibility with existing evacuated receiver technologies. The circular tube-bundle cavity design was shown to enhance optical efficiency by increasing solar absorption and reducing reflection losses compared to traditional single-tube receivers. Building upon these optical optimization results [26], the present study focuses on the thermo-hydraulic performance of the proposed receiver concept under real-scale operating conditions. A three-dimensional CFD model is developed to assess multiple tube-bundle cavity configurations and to identify the optimal design based on thermal, hydraulic, and overall efficiency criteria. In addition, a detailed thermo-hydraulic analysis of the optimal configuration is performed to clarify its flow behavior and thermal characteristics under different operating conditions.

2. New PTC receiver

This section introduces the geometry and operating principle of the proposed tube-bundle cavity receiver for parabolic trough collectors and describes the design parameters considered in the optimization process.

Fig. 1 compares a conventional PTC receiver with the proposed tube-bundle cavity configuration. In the conventional design, the receiver consists of a single absorber tube enclosed within a concentric glass envelope under vacuum. Solar radiation reflected by the parabolic mirror is focused onto the absorber, where it is transmitted through the glass envelope and absorbed by a selective coating on the tube surface. Part of the incoming radiation is lost due to optical effects at the glass envelope, while the absorbed energy is transferred to the heat transfer fluid flowing inside the tube.

As illustrated in Fig. 1b, the proposed receiver replaces the single absorber tube with multiple smaller tubes arranged in a circular bundle along the same outer circumference as the conventional design, forming a linear cavity configuration. The bundle tubes are connected to inlet and outlet manifolds (Fig. 1c), which distribute and collect the fluid while ensuring compatibility with the glass envelope and vacuum sealing. Thanks to the identical outer diameter of the manifolds and conventional absorber tubes, existing expansion bellows can be retained. In this configuration, the bundle tubes act as the primary absorbing elements, and their number and diameter are optimized to achieve a suitable trade-off between optical performance and pressure drop.

A major limitation of conventional single-tube receivers is the highly non-uniform solar flux distribution, which leads to localized hotspots on the absorber surface. These temperature gradients can induce thermal stresses, resulting in absorber tube bending and, in severe cases, glass envelope failure. The tube-bundle configuration mitigates this issue by distributing the incident solar flux among multiple smaller absorber tubes arranged within the cavity. Although local flux variations may still occur depending on the tube position, the subdivision of the absorbing surface reduces peak temperatures and temperature gradients. As a result, the receiver exhibits a more uniform thermal expansion, lowering thermally induced stresses and improving structural reliability and overall performance.

Based on the optical analysis of tube bundle receivers [25], two geometric parameters, namely the cavity opening angle (θ_c) and the cavity (r_{cavity}), can be used to identify several alternative designs (Fig. 2a). Accordingly, the overall optimization process was defined, starting from the cavity segmentation into 36 tubes (Fig. 2b). According

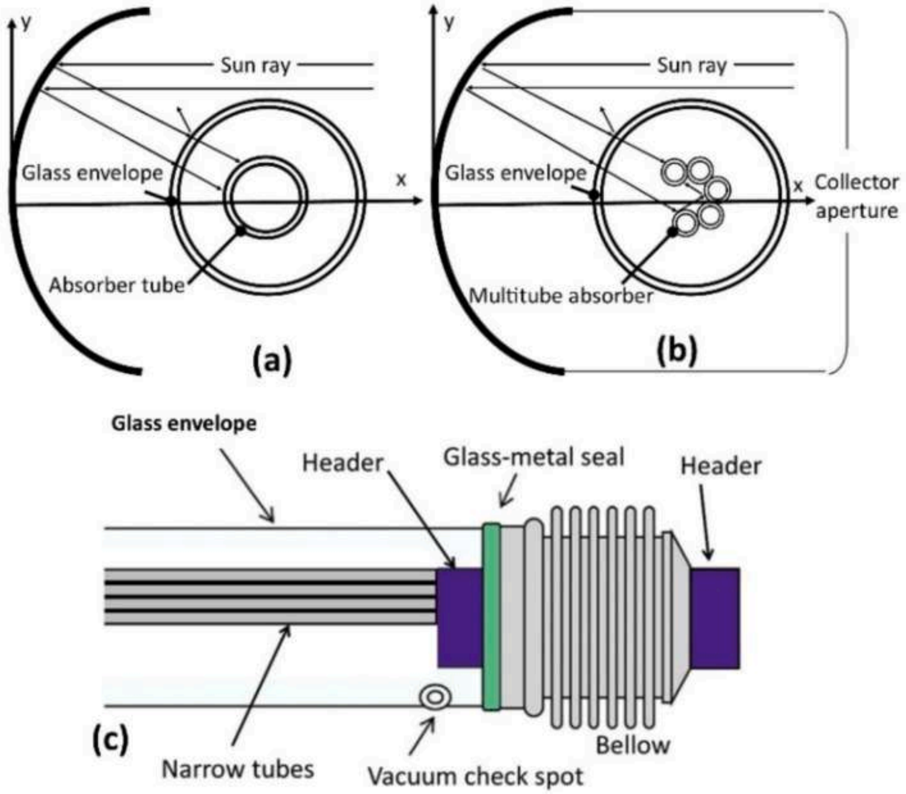

Fig. 1. Schematics of (a) a conventional PTC, (b) a PTC with cavity multi-tube, (c) structural diagram of the PTC with the cavity multi-tube absorber.

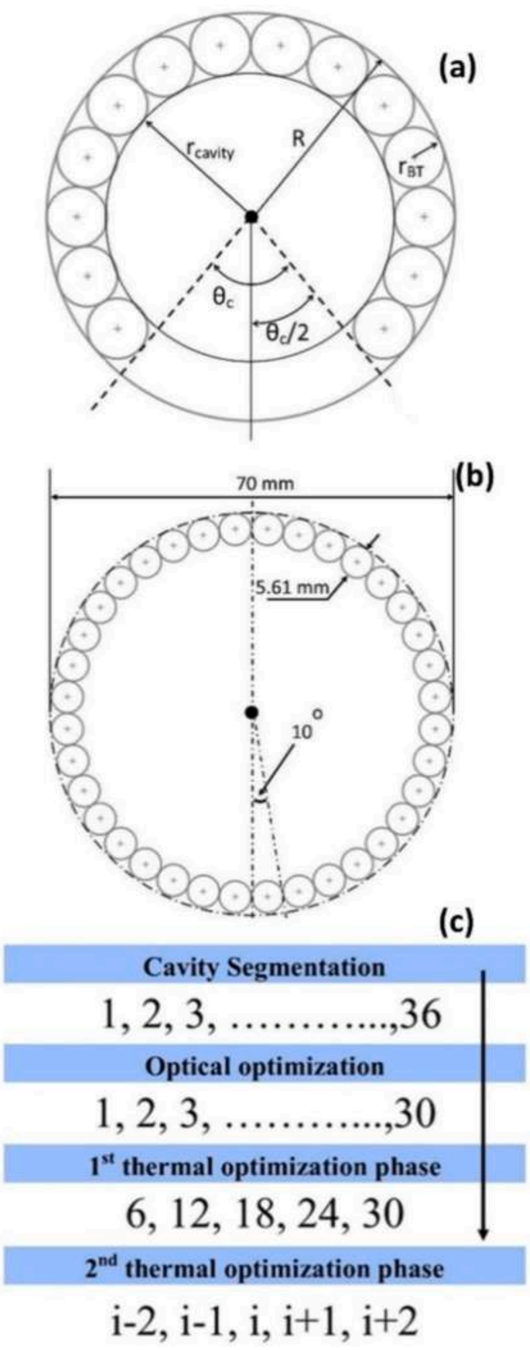

Fig. 2. Bundle configuration optimization process; (a) design parameters defined at optical optimization, (b) discretization of the model with 36 bundle tubes, (c) tube number optimization workflow.

to the results of the optical optimization phase [25], the proposed designs are characterized by a constant opening angle of $\theta_c = 60^\circ$ and different numbers of bundle tubes (BT), resulting in different values of r_{cavity}. As shown in Fig. 2c, this study integrates a two-phase thermal optimization process into the previously obtained optical results. In the first phase, tube numbers are varied in steps of six, leading to five design options with 6, 12, 18, 24, and 30 tubes. In the second phase, once the configuration providing the maximum performance is identified, neighboring designs are further assessed to cover all possible options tube-number variations. In this context, Fig. 3 illustrates the five different configurations investigated at the first optimization level. It should be noted that the layouts shown in Fig. 3 are simplified half-geometry representations, due to the symmetrical nature of the PTC designs. Table 1 summarizes the corresponding design parameters for each configuration.

The receiver design was made based on one of the parabolic trough collectors installed in the HTF Test Loop planned for the experimental validation of new solar components at the Plataforma Solar de Almería (PSA), located in the Tabernas desert (Spain). The targeted test configuration consists of an east–west oriented PTC. The collector technology adopted is the UrssaTrough, and the receiver tubes used correspond to the PTR®70 model, manufactured by Schott. The UrssaTrough collector features a parabolic aperture width of 5.76 m and a total length of 150 m. The installed prototype, arranged in a half-collector configuration, consists of six solar collector assemblies (SCAs) with a length of 12 m each, and a total receiver length of 184 m of PTR®70 tubes. This configuration results in a net collecting area of 409.9 m^2 [26].

The entire optimization process was based on Fig. 3, starting from the cavity segmentation into 36 tubes, which resulted in a maximum of 30 tubes after the optical optimization. In this study, two thermal optimization phases are then integrated into the previously obtained results. In the first phase, tube numbers are varied in steps of six, resulting in five design options with 6, 12, 18, 24, and 30 tubes. In the second phase, once the configuration providing the maximum performance is identified, neighboring designs are further assessed to cover all possible tube-number variations.

To numerically evaluate the proposed designs, simulations were conducted based on a case study reported in [26]. Initially, a conventional PTR®70 receiver was modeled, and the numerical results were compared with the corresponding experimental data. After validating the numerical models, simulations of the proposed receivers were performed using the same thermal models and boundary conditions to assess the potential of replacing conventional systems with the new designs. The main parameters of the reference system are listed in Table 2.

3. Numerical modelling

3.1. Thermal model

The first step in thermal modeling consists in evaluating the solar heat flux incident on the absorber. In the case of PTC, the total concentrated solar irradiance reaching the receiver is expressed as.

$$E_{(S-con)} = LCR \times IAM \times DNI \quad (1)$$

where *DNI* is the maximum solar incident, and *IAM* is the incident angle modifier (equal to 1 in this study, since a normal incidence angle of 0° is considered), and *LCR* denotes local concentration ratio. The latter is obtained from optical simulations by evaluating the fraction of solar rays reflected by the concentrator and reaching the absorber surface. Accordingly, for the tube-bundle configurations, LCR values are determined for each individual tube using optical simulations [25] and applied to the corresponding pipe, as illustrated in Fig. 4.

The absorbed solar power is calculated as a function of the absorber absorptivity coefficient (α) according to

$$E_{(S-abs)} = \alpha E_{(S-con)} \quad (2)$$

The useful thermal power, E_u, is then defined as the fraction of absorbed solar energy that remains after thermal losses,

$$E_u = E_{(S-abs)} - E_{loss,th} \quad (3)$$

where $E_{loss,th}$ represents the total thermal losses from the absorber to the ambient, which include convective losses $E_{loss,\ conv}$ (Eq. (4)) and radiative losses $E_{loss,\ rad}$ (Eq. (5)). Conduction losses to the experimental support structure are neglected. Convective heat losses are calculated as

$$E_{loss,\ conv} = A_p h_w \left(T_p - T_{amb}\right) \quad (4)$$

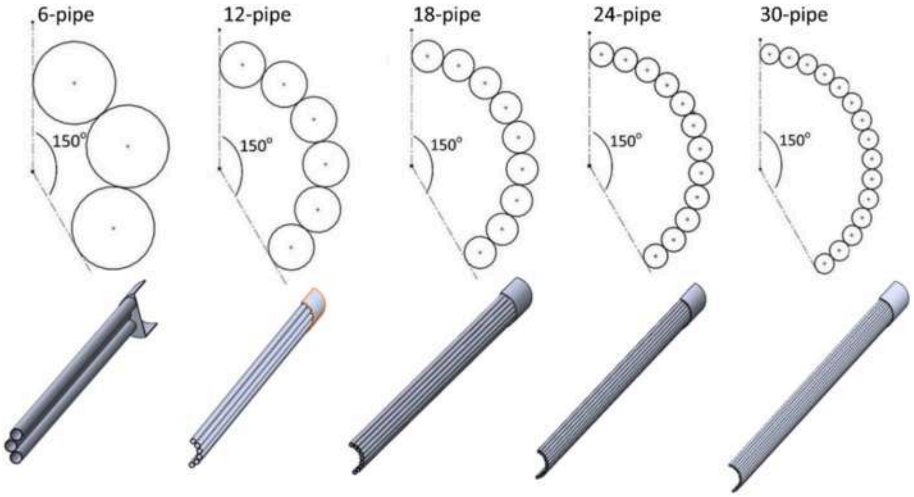

Fig. 3. Various bundle-cavity receiver designs developed and assessed at first thermal optimization phase (note that the CAD files are shown as half-geometry).

Table 1
Geometrical parameters of the designs studied at the first thermal optimization phase.

Model	Number of tubes	BT inner diameter (mm)	BT Thickness (mm)
6-pipe	6	17.63	1.5
12-pipe	12	9.46	1.5
18-pipe	18	5.86	1.5
24-pipe	24	3.87	1.5
30-pipe	30	3.61	1

Table 2
Specification of the experimental test facility and parameters.

Parameters	Symbol	Value
Solar collector aperture width	W	5.76 m
Solar collector focal length	foc	1.71 m
Receiver length	L	4 m
Absorber tube outer diameter	D_{po}	0.07 m
Absorber tube inner diameter	D_{pi}	0.066 m
Glass tube outer diameter	D_{go}	0.125 m
Absorber tube absorptivity	α_p	0.93
Absorber tube emittance	ε_p	0.14
Glass tube transmissivity	τ_g	0.96
Glass tube absorptivity	α_g	0.02
Parabola specular reflectivity	ρ_r	0.93
Incidence angle	Φ_{inc}	0.0°
Heat transfer fluid	HTF	Syltherm^{TM}800
Solar collector optical efficiency	η_{opt}	0.768
Fluid inlet temperature	T_{in}	400 K
Fluid flow rate	$\dot{m}$	15 m^3/h
Ambient temperature	T_{amb}	300 K
Direct normal irradiance	DNI	864 W/m^2

where A_p is the outer surface area of the absorber, h_w is the wind heat transfer coefficient (assumed equal to 20 W/m^{2}K), while T_p and T_{amb} are the absorber and ambient temperatures, respectively.

Radiative heat losses are given by

$$E_{loss,\ rad} = \mathrm{A}_p\sigma\varepsilon_p(T_p^4 - T_{sky}^4) \tag{5}$$

where σ is the Stefan–Boltzmann constant, ε_p is the absorber emissivity, and T_{sky} is the effective sky temperature, estimated for clear-sky conditions as $T_{sky} = 0.0553\,T_{amb}^{1.5}$ according to Ref. [27]. The energetic efficiency of the absorber is defined as the ratio between the useful thermal power and the total concentrated solar power reaching the absorber:

$$\eta_{en} = \frac{E_u}{E_{(S-\mathrm{con})}} \tag{6}$$

To account for the increased pumping power associated with geometrical modifications of the absorber, an overall efficiency is defined as [28].

$$\eta_{ovr} = \frac{E_u - \frac{W_p}{\eta_{el}}}{E_{(S-\mathrm{con})}} \tag{7}$$

where W_p is the pumping work requirement, calculated as

$$W_p = \frac{\dot{m}\Delta p}{\rho} \tag{8}$$

and $\eta_{el} = 32.7\%$ represents the combined efficiency of the power block, electrical generator, and circulation pump. Including the pumping power penalty in the efficiency definition ensures that the optimization process does not artificially favor configurations with enhanced heat transfer at the expense of excessive pressure losses[29].

Finally, a temperature uniformity index is introduced to quantify the distribution of temperature on fluid or solid surfaces. The index is defined as

$$Uniformity index of T = 1 - \frac{\sum |T_f - \overline{T}| A_f}{2|\overline{T}|\sum A_f} \tag{9}$$

where $\overline{T}$ is the surface average of temperature, T_f is the local face temperature, and A_f is the corresponding face area.

3.2. Numerical setup

Simulations were carried out using a thermo-hydraulic model developed in the commercial Star-CCM + software. As shown in Fig. 5, the computational domain consists of the glass envelope, absorber tubes, manifolds, and heat transfer fluid (HTF). The solar receiver was modeled under three-dimensional, steady-state, turbulent flow conditions. Accordingly, a steady-state conjugate heat transfer approach was adopted to resolve the thermal interaction between solid and fluid regions. Radiative heat transfer was modeled by applying a *surface-to-surface* radiation model to the surfaces of the absorber tubes and glass envelope. In addition, the radiation model accounts for radiation, reflection, refraction, and convective heat losses from the glass envelope to the ambient environment. Radiation transfer options were set as *external* for the absorber tubes and *internal-and-external* for the glass

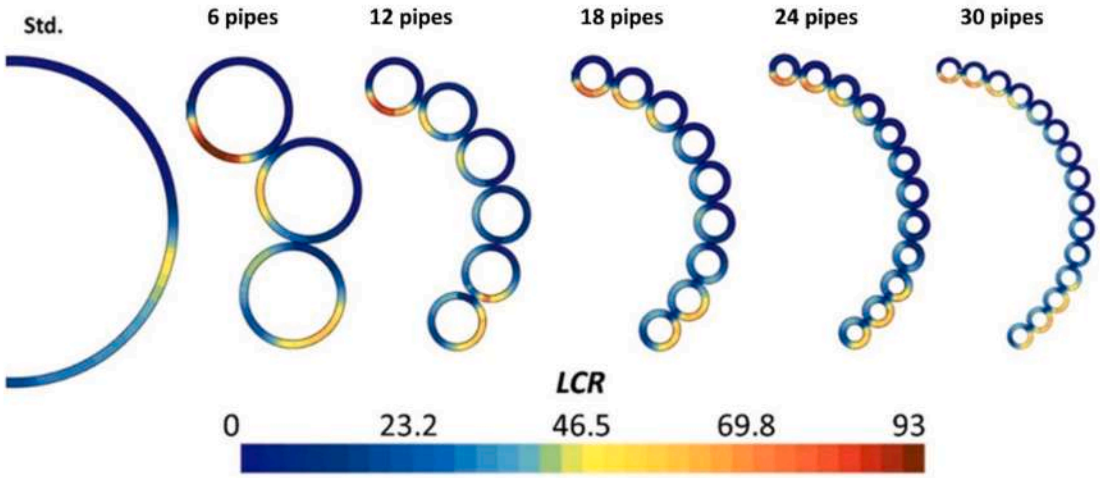

Fig. 4. Solar flux distribution determined in terms of LCR for all receiver designs.

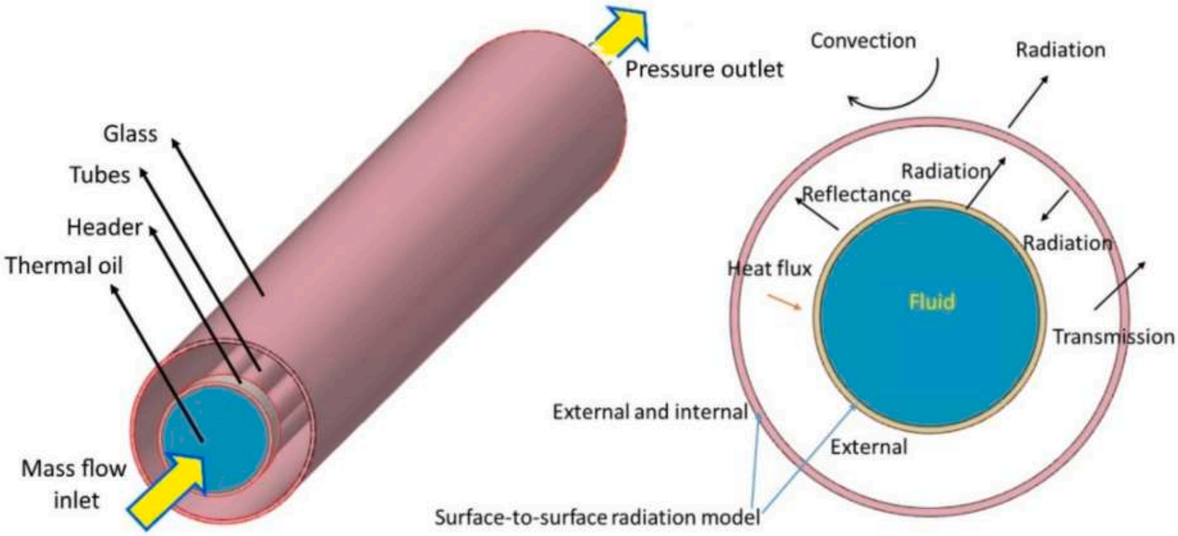

Fig. 5. Physical model and boundary conditions applied to tubular samples.

envelope.

The heat transfer fluid (Syltherm^{TM} 800) was modelled using temperature-dependent thermophysical properties. Turbulent flow inside the receiver was simulated using a two-equation Reynolds-Averaged Navier–Stokes (RANS) model, specifically the two-layer realizable k-ε model with an all-y$^+$ wall treatment. The two-layer formulation enables an automatic transition between low-y$^+$ and high-y$^+$ wall treatments, providing flexibility across different mesh resolutions.

The solid regions, including the glass envelope and absorber tubes, were solved using a segregated solid energy equation, with thermal conductivity, specific heat capacity, and density defined as temperature-dependent properties. Solar heat flux distributions were applied to the outer surfaces of the absorber tubes through user-defined field functions derived from Monte Carlo ray-tracing simulations. A mass flow rate boundary condition was imposed at the inlet, while a pressure outlet condition was specified at the outlet. The complete set of boundary conditions adopted in the numerical model is illustrated in Fig. 5 for the proposed absorber configuration.

3.3. *Grid sensitivity analysis*

In this study, a hybrid meshing strategy combining structured and unstructured elements was adopted to generate a reliable computational grid for the solution domain. Polyhedral cells with prismatic layers in the fluid regions were employed to resolve the governing equations. To ensure that the numerical results are independent of the mesh resolution, a grid sensitivity analysis was performed for all the investigated cases. Grid refinement was carried out by initially assigning a constant base cell size and progressively refining the mesh until a wall-adjacent resolution corresponding to $y^+ \approx 1$ was achieved. Subsequently, the number of prismatic layers was kept constant, and further refinement was performed by reducing the base cell size until convergence of the results was obtained. As a result, four different mesh levels were generated for each configuration, ranging from a coarse grid to a fine reference mesh. The details of the grid sensitivity analysis for all cases are reported in Appendix A.

3.4. *Validation*

To evaluate the accuracy of the developed mesh and the employed physical models over the investigated Reynolds number range, a standard receiver configuration was simulated using a constant heat flux of 1000 W/m^2 and different Reynolds numbers. The numerical results were compared with standard empirical correlations in terms of the Nusselt number (*Nu*) and friction factor (*f*). The relevant dimensionless parameters, including the Reynolds and Nusselt numbers, are defined as [30].

$$Re = \frac{4\dot{m}}{\pi D_i \mu} \tag{10}$$

$$Nu = \frac{E}{\pi L k (T_{wall} - \overline{T_f})} \tag{11}$$

where T_{wall} is the average wall temperature obtained at the fluid–solid interface. The friction factor was computed under isothermal flow conditions according to

$$f = \frac{2}{L/D_{\mathrm{pi}}} \frac{\Delta p}{\rho \overline{v}^2} \tag{12}$$

As shown in Fig. 6a, the friction factor values predicted by the present CFD model are compared with the Petukhov correlation [31] over the range $20,000 < \mathrm{Re} < 110,000$, showing an average deviation of approximately 2%, which is within the acceptable accuracy of the correlation. Similarly, Fig. 6b presents the comparison between the CFD-predicted Nusselt numbers and the Dittus–Boelter correlation [32], with an average deviation below 5%. This level of agreement confirms the suitability of the adopted numerical models for performance assessment within the investigated Reynolds number range.

To further validate the numerical framework against experimental data, the simulation results were compared with measurements reported in Ref.[26] for the standard receiver design. The comparison was first conducted in terms of thermal efficiency and subsequently extended to the heat loss per unit receiver length in order to assess the accuracy of the radiation models applied to the absorber tube and glass envelope. Fig. 7 shows the comparison between experimental and numerical results for both metrics as a function of the temperature difference ΔT, defined as the difference between the average fluid temperature and the ambient temperature. The numerical predictions are in good agreement with the experimental data and remain within the experimental uncertainty bounds, demonstrating the capability of the developed CFD model to accurately reproduce real operating conditions.

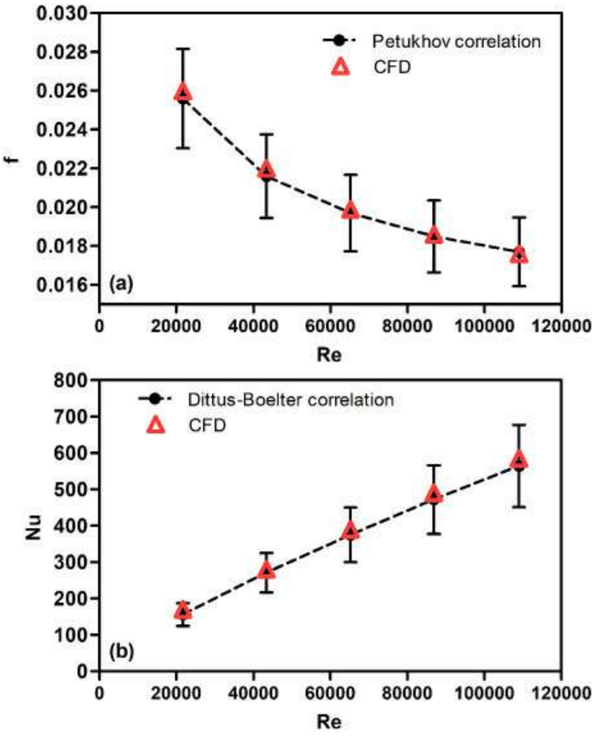

Fig. 6. Comparison of f and Nu for Std. design between the developed CFD models and standard correlations.

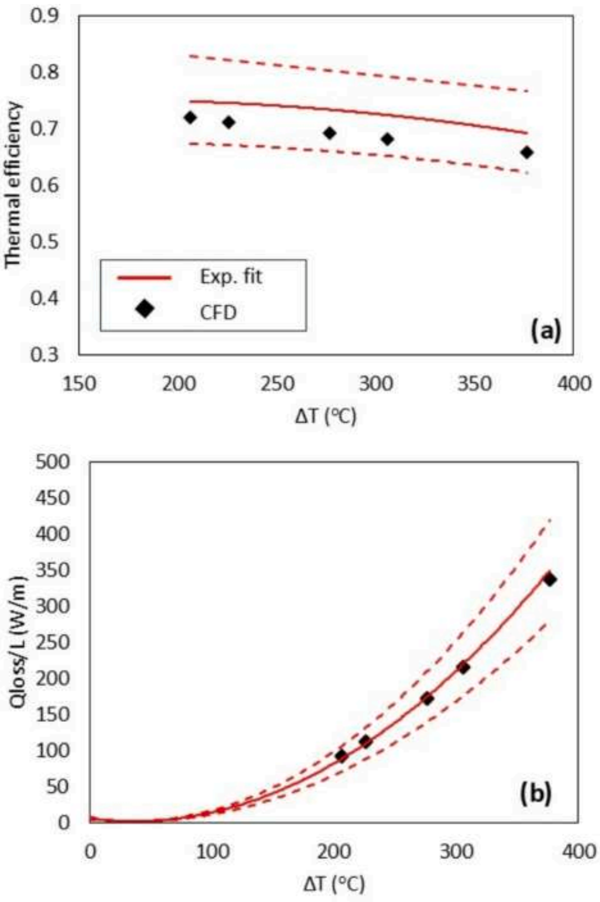

Fig. 7. Validation of the numerical study against the experimental test data [26] in terms of (a) collector thermal efficiency, (b) heat loss per receiver length.

4. Results and discussions

4.1. Comparative study

4.1.1. Hydraulic characteristics

In this section, a comparative analysis is performed to identify the optimal tube-bundle configuration. With respect to the hydraulic performance of the different designs, Fig. 8a illustrates the flow distribution from the inlet header to the bundle tubes, using velocity streamlines for the 18-pipe configuration, showing an almost uniform flow split among the tubes. To quantify the associated pressure losses, Fig. 8b reports the pressure drop computed along the receiver for the various configurations. As expected, reducing the tube diameter increases the flow resistance inside the bundle tubes, despite the lower mass flow rate in each individual pipe. This effect results in a significant increase in pressure drop, which rises from approximately 700 Pa for the standard design to about 3.5×10^6 Pa for the 30-pipe configuration.

4.1.2. Receiver temperature

When the heat fluxes described in Fig. 3 are applied, the temperature field shown in Fig. 9 is computed on a cross-sectional plane located at

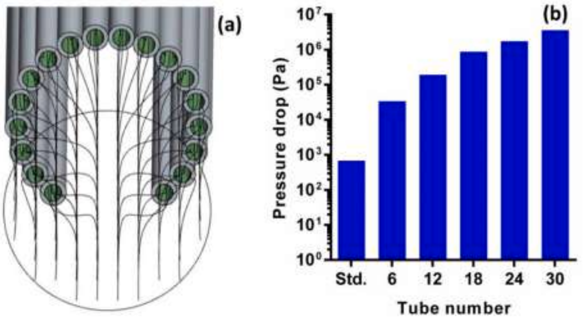

Fig. 8. (a) Fluid streamlines for the flow between the header and bundle tubes (18-pipe case), (b) pressure drop computed for various designs.

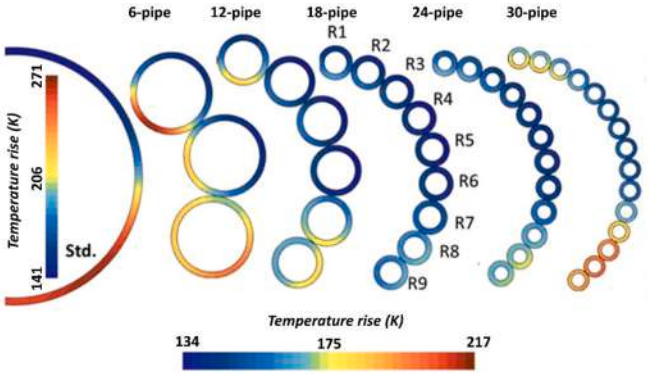

Fig. 9. Temperature field computed on a cross-sectional plane created at the receiver middle length (Z = 2 m) for all studied PTCs.

the midpoint (Z = 2 m), where the tube temperature rise reaches up to 271 K in the standard design (Std.). It should be noted that analyses conducted at $Z = 2$ m are of particular relevance, as the maximum temperature-induced deflection typically occurs at this location [33], which is therefore commonly referred to as the critical segment. The temperature distributions on the tube walls of all tube-bundle designs at the same axial location indicate that the bundle configuration significantly reduces the solid temperature, with a decrease of nearly 50 K compared to the standard design. An analysis of the 13-pipe configuration, taken as a representative example, shows that the maximum surface temperature occurs on tube R8, which is subjected to two distinct solar flux contributions, as illustrated in Fig. 3. The tubes located in the lower part of the cavity (i.e., R9, R8, and R7) experience two local flux peaks: one originating from the external reflectors and one from the internal cavity surfaces (see also Refs. [25;24]). Further analysis reveals that the location of the hotspot varies with the tube-bundle configuration. For instance, in the 6-pipe design, the hotspot is observed on the upper tube (R1), whereas in the 12-pipe configuration, tubes R1, R5, and R6 exhibit the highest surface temperatures. As the number of bundle tubes increases, the hotspot progressively shifts toward the lower tubes.

To compare the various bundle designs, Fig. 10a illustrates the hotspot temperature rise, defined with respect to the average fluid temperature (approximately 130 K), for each configuration. All the proposed bundle designs exhibit a reduction in absorber hotspot temperature compared to the standard case, confirming the thermal enhancement achieved by the proposed concept. This behavior can be attributed to the increased fluid velocity inside the absorber tubes, together with the larger effective heat transfer area provided by the bundle configuration. Among the investigated layouts, the 18-pipe design exhibits the lowest hotspot temperature, indicating a favorable balance between solar flux concentration and internal fluid flow. In more detail, Fig. 10b presents the temperature uniformity index computed for the tube wall temperature rise in each design. The results show that the tube-bundle configuration increases temperature uniformity by up to 23%, with the maximum uniformity achieved by the 30-pipe design. This indicates that the bundle cavity arrangement effectively mitigates both radial and circumferential temperature gradients, resulting in a more uniform wall temperature distribution. Such an improvement in temperature uniformity not only enhances the overall thermal behavior of the collector but also implies reduced thermal stresses, which are expected to contribute to increased operational reliability and longer service life compared to the standard single-tube receiver.

4.1.3. *Overall performance*

Fig. 11 summarizes the performance metrics evaluated for each receiver configuration. As shown in Fig. 11a, the thermal efficiency is enhanced for all tube-bundle designs, indicating that the cavity arrangement of bundle tubes promotes higher heat transfer rates between the solid and fluid regions, while reducing thermal losses due to lower absorber surface temperatures. As the number of tubes increases, or equivalently as the individual tube diameter decreases, the thermal efficiency improves, reaching a maximum value of approximately 0.98 for the 30-pipe configuration. However, as discussed in Fig. 8, this improvement is accompanied by a substantial increase in pressure drop, which results in a higher pumping power demand. The resulting overall efficiency, accounting for both thermal gains and hydraulic penalties, is shown in Fig. 11b. The standard configuration (Std.) exhibits nearly identical values of thermal and overall efficiency due to its negligible pressure drop. The 6-pipe and 12-pipe designs slightly outperform the

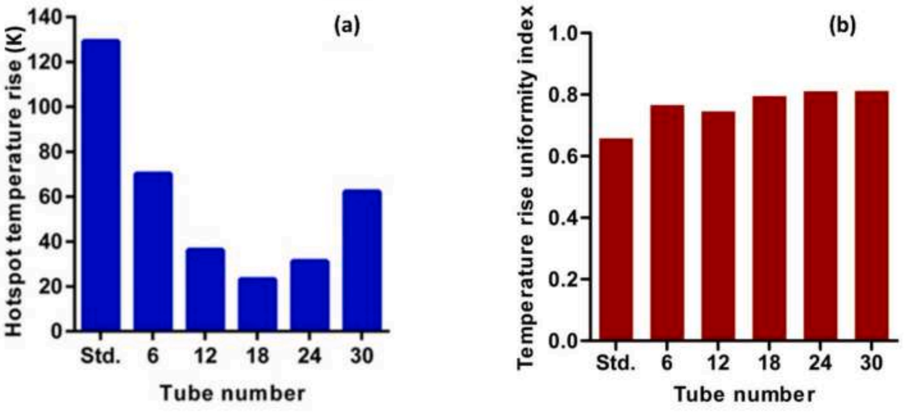

Fig. 10. (a) hotspot temperature rise and (b)temperature rise uniformity index computed for various designs.

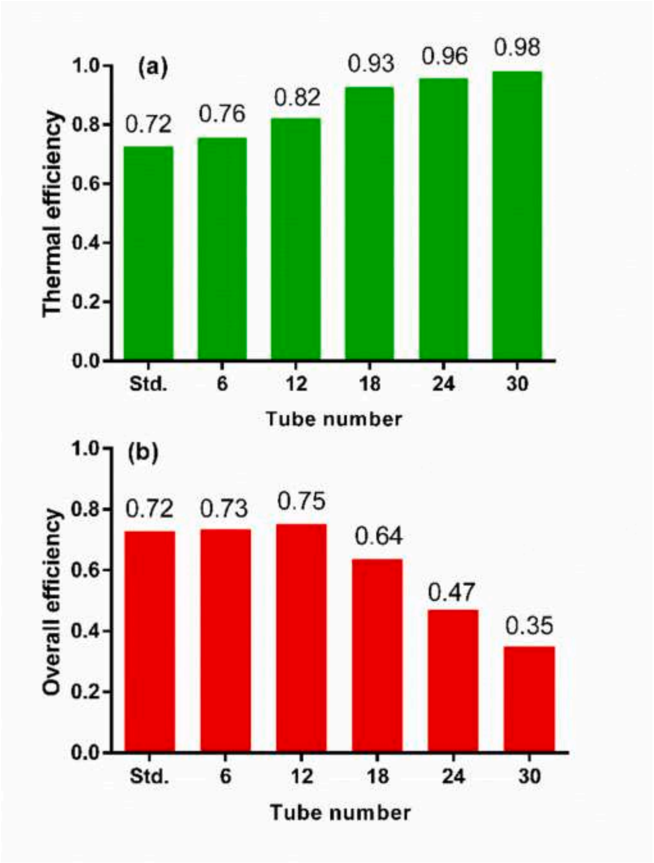

Fig. 11. Performance evaluation for the receiver designs in terms of (a) thermal and (b) overall efficiency based on the inputs from Table 1.

standard case in terms of overall efficiency, whereas for the remaining configurations, the increased pressure losses outweigh the thermal enhancement, leading to lower overall efficiencies than the standard design. As a consequence, the 12-pipe configuration, providing an overall efficiency increase of approximately 4% relative to the standard receiver, is identified as the optimal design for the investigated operating range (average fluid temperature of 402.8 K). In the subsequent step, additional configurations with geometrical constraints similar to those of the 12-pipe design are further examined to determine the final optimized layout.

To increase the resolution of the investigated design space within the comparative framework, additional neighboring configurations were further examined. Accordingly, four new designs with 10, 11, 13, and 14 tubes were analyzed. Table 3 summarizes the geometric parameters of the configurations considered at this second optimization stage.

As shown in Fig. 12, the performance of the additional configurations is compared with that obtained in the previous optimization phase. In terms of thermal efficiency, the 12-tube configuration continues to outperform the neighboring designs. When the effects of pressure drop are also taken into account, a maximum overall efficiency of approximately 0.75 is achieved, confirming that the 12-tube configuration represents the optimal design among the investigated tube-bundle layouts.

Table 3
Geometrical parameters of the designs studied at the second thermal optimization phase.

Model	Number of tubes	BT inner diameter (mm)	BT Thickness (mm)
10-pipe	10	11.39	1.5
11-pipe	11	10.35	1.5
13-pipe	13	8.67	1.5
14-pipe	14	7.97	1.5

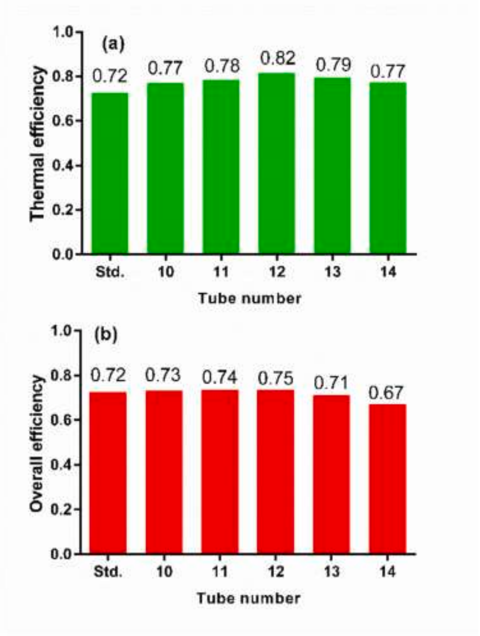

Fig. 12. 2nd level of performance evaluation for the receiver designs in terms of (a) thermal and (b) overall efficiency.

4.2. *Detailed thermo-hydraulic analyses*

This section focuses on the hydraulic and thermal performance of the optimal 12-pipe configuration by considering four different fluid inlet temperatures and analyzing the resulting flow and thermal characteristics within the absorber.

4.2.1. *Hydraulic performance*

As shown in Fig. 13a, the velocity profiles are extracted on a cross-sectional plane at the absorber outlet for an inlet temperature of $T_i =$ 400 K. The velocity distributions at the manifold outlet exhibit a symmetric behavior between the six left-hand and six right-hand tubes, indicating that the manifolds distribute the flow uniformly among the bundle tubes. Under heated operating conditions, each BT is subjected to a different solar heat flux, resulting in non-uniform tube wall temperatures. Consequently, the heat transfer fluid experiences different temperature levels and viscosity variations as it flows through each tube. This leads to unequal hydraulic resistance among the BTs and, therefore, to different velocity profiles. In particular, tubes L/R1, L/R5, and L/R6 exhibit higher velocity values than the remaining BTs, which can be attributed to the higher solar flux concentrations on these tubes (Fig. 8) and the associated reduction in fluid viscosity. Furthermore, velocity fields obtained from longitudinal cross sections on manifolds reveal the formation of a reverse flow region in the space below the fluid discharge from the BTs. This reverse flow is more pronounced beneath the R1 outlet and gradually weakens toward the other tubes. Fig. 13b shows the corresponding velocity streamlines at the outlet manifold, highlighting the development of this secondary flow within the void region. Such secondary flow promotes thermal mixing, leading to a more uniform fluid temperature distribution at the outlet face.

To further examine the effects of heating on flow distribution, Fig. 14 presents the mass flow rates in the bundle tubes under different operating conditions. As expected, the non-heated absorber exhibits a uniform flow distribution among the BTs. The results also show that non-uniform heating of the individual BTs leads to an uneven flow split. In particular, tubes L/R2, L/R3, and L/R4, which are subjected to the

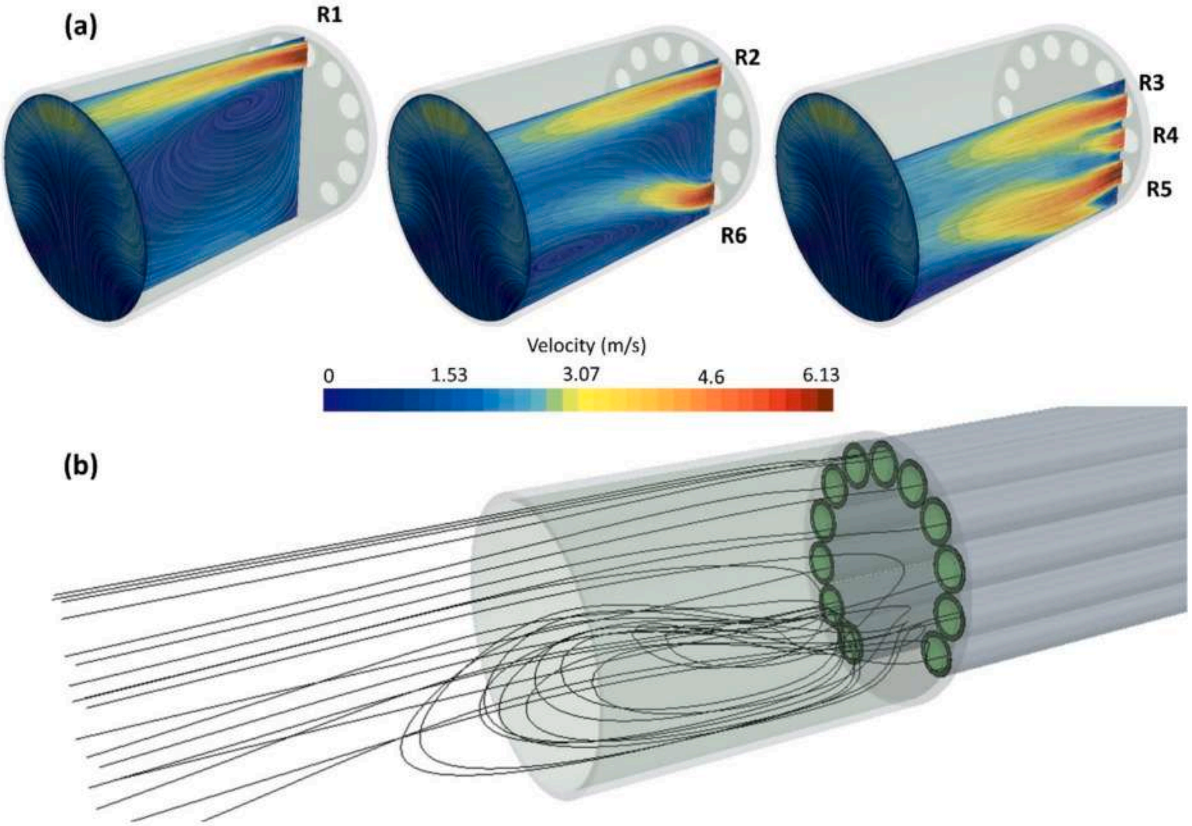

Fig. 13. Velocity profiles computed on the outlet manifold of the absorber: (a) velocity contours at different tube outlets and (b) fluid streamlines.

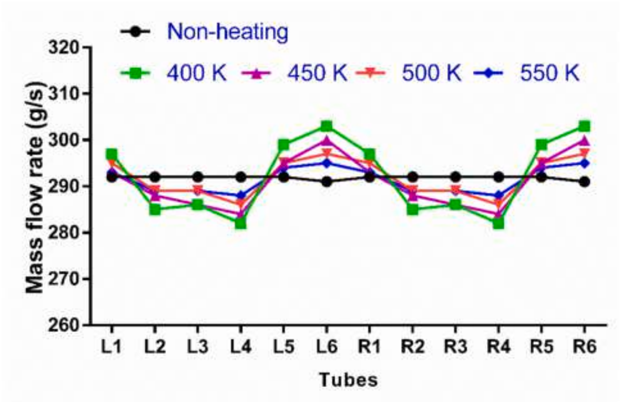

Fig. 14. Fluid flow distribution computed for all investigated conditions.

lowest solar flux concentrations, receive the smallest fraction of the total mass flow, with values lower than those observed in the non-heated case. Conversely, as previously discussed, tubes L/R1, L/R5, and L/R6 exhibit higher mass flow rates than the non-heated configuration. An analysis of different fluid inlet temperatures indicates that increasing the inlet temperature reduces the non-uniformity of the mass flow distribution among the BTs. This behavior can be attributed to the smaller temperature rise between the inlet and outlet at higher inlet temperatures, which results in reduced viscosity variations and, consequently, more uniform hydraulic resistance. Under these conditions, the maximum mass flow rate is observed in tubes L/R6, reaching approximately 300 g/s at an inlet temperature of 400 K, while the minimum value of about 280 g/s occurs in tubes L/R4 under the same operating conditions.

The second hydraulic characteristic investigated is the fluid pressure drop occurring between the inlet and outlet manifolds. Fig. 15 illustrates the pressure drop distribution computed for an inlet temperature of 400 K, showing how the total pressure loss is apportioned among the two manifolds and the BTs. The results indicate that, when the absorber is divided into three main sections, the BT region, which includes the narrow tubes, accounts for nearly 94% of the total pressure drop, representing the primary contributor to the pumping power demand. In contrast, the inlet and outlet manifold sections contribute only about 2% and 4% of the total pressure drop, respectively.

To investigate the influence of inlet temperature on the pressure drop across the absorber, Fig. 16 presents the computed pressure losses under different operating conditions. Since the thermophysical properties of the heat transfer fluid are temperature dependent, heated operating conditions result in lower pressure drops compared to non-heated conditions due to the reduced fluid viscosity. Overall, heating leads to a reduction in pressure drop of nearly 50%. When comparing the different inlet temperatures, the lowest pressure drop is obtained at an inlet temperature of 550 K, which can be attributed to the lower viscosity levels achieved under this operating condition.

4.2.2. *Thermal performance*

This section examines the thermal behavior of the absorber, focusing on the temperature distribution in both the fluid and solid regions. In this context, Fig. 17 shows the fluid temperature rise at the outlet surface for the different inlet temperature conditions investigated.

As shown, the tube-bundle configuration promotes thermal mixing at the outlet manifold, resulting in a fluid temperature range (defined as the difference between the maximum and minimum values) of approximately 10 K for the proposed design, compared with about 120 K for the standard receiver. This clearly demonstrates how the bundle configuration enhances thermal mixing in the manifolds and leads to a more uniform temperature distribution at the outlet. Furthermore, increasing

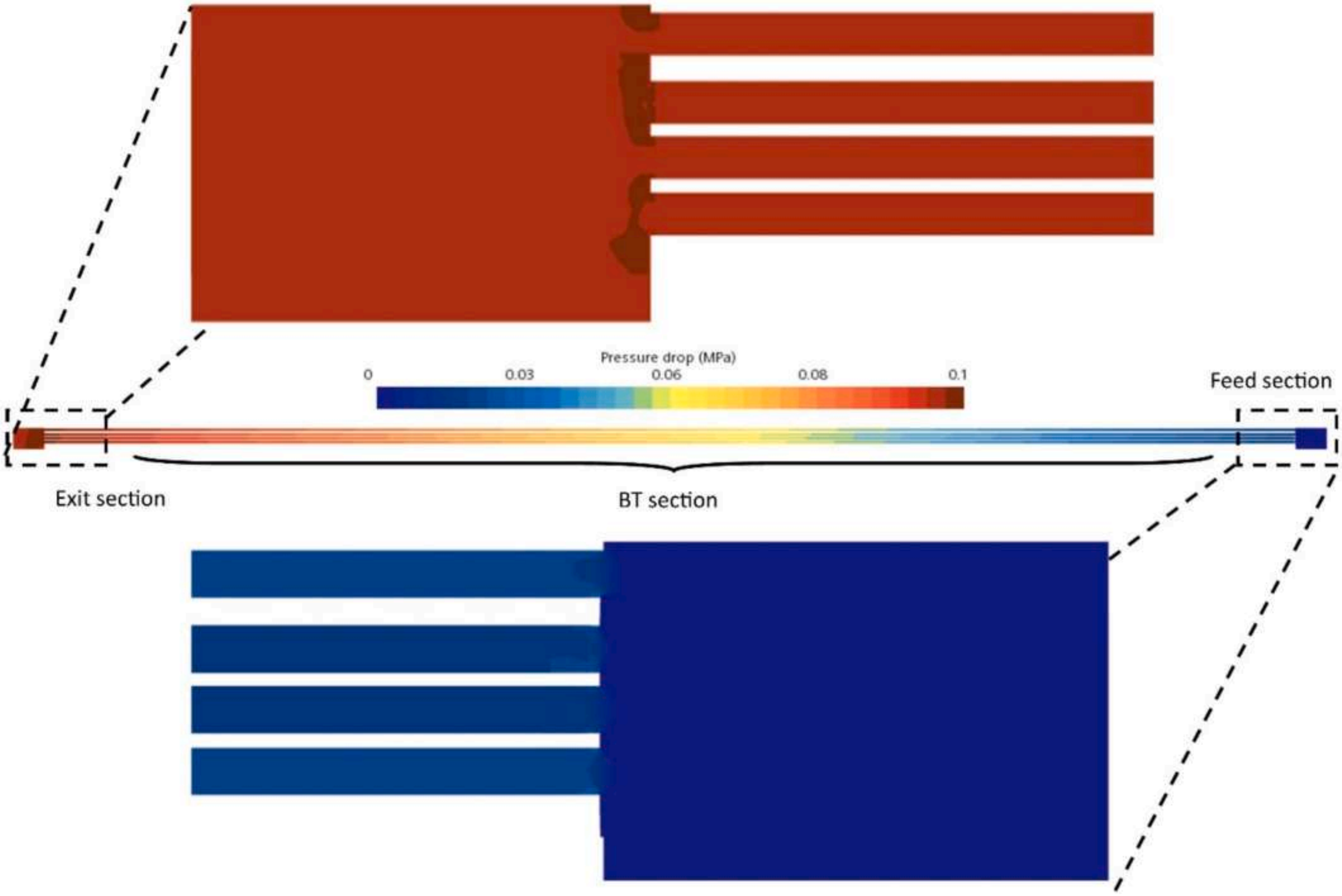

Fig. 15. Pressure drop map computed for the absorber with 400 K inlet temperature.

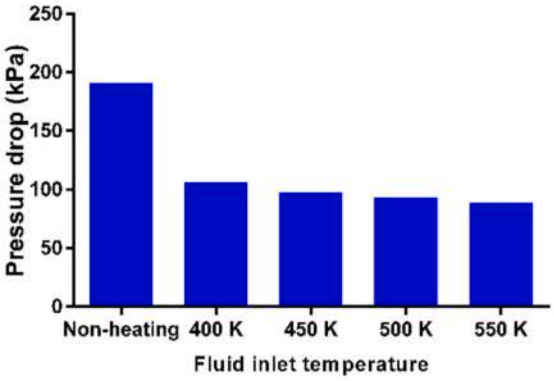

Fig. 16. Pressure drop map values obtained at different working conditions.

the inlet temperature reduces the temperature rise at the outlet surface, indicating a lower heat transfer rate under these conditions due to the reduced temperature gradient between the solid and fluid regions. An analysis of the outlet temperature field shows that the lower section of the manifold is warmer and primarily influenced by the highly irradiated bundle tubes, namely L/R5 and L/R6, which deliver higher fluid temperatures. A localized hotspot is also observed near the tube segment corresponding to L/R1, which receives a high solar flux contribution from the internal side of the cavity.

Fig. 18a presents the tube wall temperature maps obtained on different longitudinal cross sections, illustrating the axial development of wall temperatures for both the proposed and conventional absorbers operating at an inlet temperature of $T_i = 400$ K. The values are reported as temperature rises relative to the fluid inlet temperature. As shown, the tube-bundle configuration results in significantly lower tube wall temperature rises compared to the standard single-tube design. In both configurations, the tube wall temperature increases along the flow direction, indicating a reduced heat transfer tendency in the downstream region as the fluid temperature rises. The circumferential temperature profiles at $Z = 2$ m are further analyzed in Fig. 18b, which shows the temperature distribution around the tubes for both the tube-bundle and standard designs. Here, Y denotes the vertical position on the absorber tube (with $D_{po} = 70$ mm). Owing to the symmetry of the temperature distribution, only half of the geometry is considered. The figure compares the circumferential temperature profiles of each BT with the corresponding position on the standard absorber tube. One of the main observations is that the temperature non-uniformity is substantially lower in the tube-bundle configuration than in the standard receiver. Among the bundle tubes, L1 exhibits the largest temperature variation, with a range of approximately 40 K, which is still about 70% lower than that of the standard tube. For $Y < 10$ mm, tube L1 reaches higher temperatures than the standard design due to the cavity effect in the tube-bundle configuration, where solar radiation is concentrated from the internal side of the cavity. In contrast, the corresponding region in the standard receiver is exposed only to direct solar radiation and remains below a temperature rise of 20 K. For $Y > 40$ mm, the standard receiver experiences a sharp temperature increase of up to 150 K, whereas tubes L5 and L6 exhibit moderate temperature rises of up to about 60 K due to the redistribution of the solar flux among the bundle tubes.

To further quantify hotspot behavior, hotspot temperature values

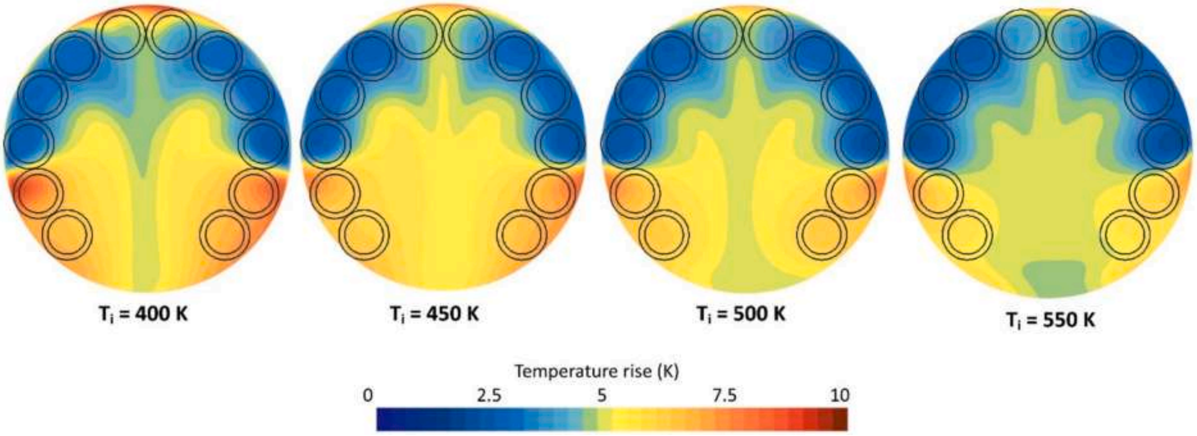

Fig. 17. Temperature values obtained at the outlet of the manifold with different working conditions.

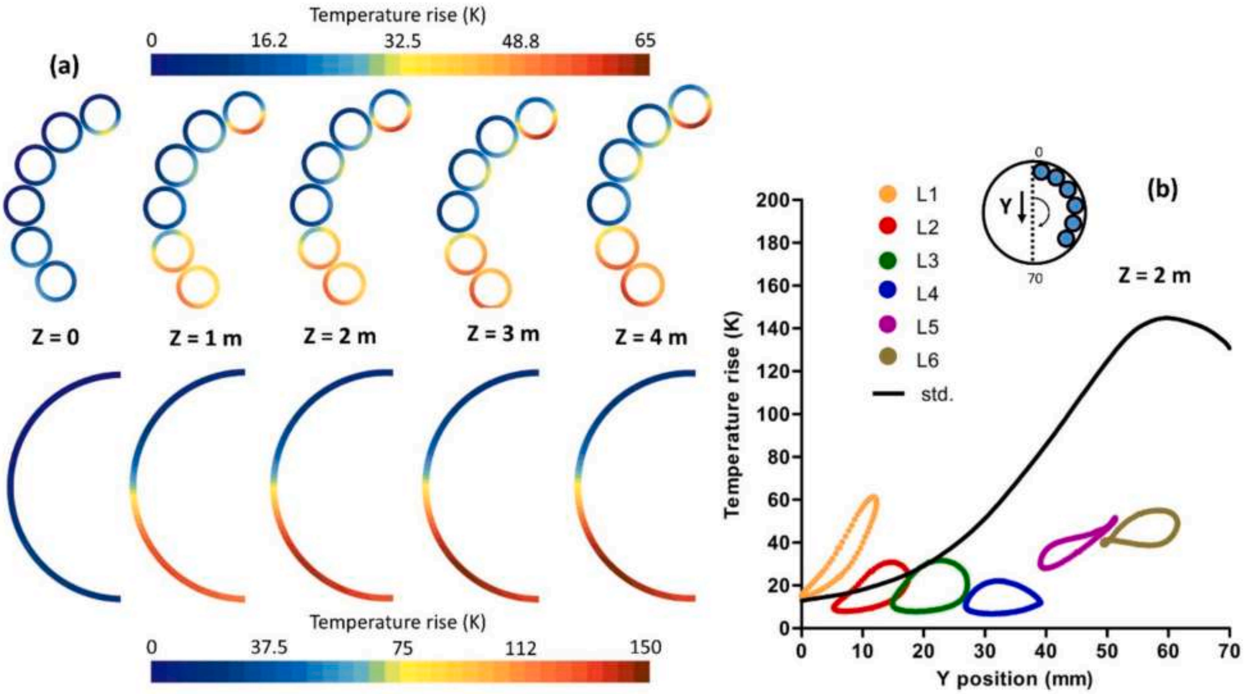

Fig. 18. Temperature profiles obtained for the new and the conventional absorber working at Ti = 400 K, analyzing (a) different longitudinal cross sections, (b) circumferential temperature distribution at Z = 2 m.

were extracted for different inlet temperatures, as shown in Fig. 19. The results indicate that the proposed tube-bundle configuration is effective in reducing hotspot temperatures compared to the standard design. This confirms that the redistribution of the solar heat flux among the BTs, inherent to the tube-bundle cavity configuration, represents an effective strategy for mitigating hotspot formation in PTCs. Among the bundle tubes, L1 exhibits the highest hotspot temperature; nevertheless, it still achieves a reduction in hotspot temperature rise of approximately 57% at $T_i = 400$ K and 46% at $T_i = 550$ K relative to the standard receiver. Furthermore, increasing the fluid inlet temperature leads to a reduction in the hotspot temperature rise. This behavior indicates that, although the heat transfer fluid operates at higher temperatures, the tube wall temperature increases at a lower rate than T_i, resulting in a smaller temperature difference.

The thermal performance of the receiver is evaluated in terms of thermal and overall efficiencies, as shown in Fig. 20. According to Fig. 20a, the thermal efficiencies obtained for the novel TB design demonstrate the superiority of this absorber compared to the conventional receiver over the entire range of investigated fluid inlet temperatures. In particular, an increase of approximately 8% in thermal efficiency is achieved by the TB absorber relative to the standard tube at an inlet temperature of 400 K. When considering the effect of varying inlet temperatures, the results show that the thermal efficiency slightly decreases as T_i increases. This trend can be attributed to the larger temperature difference between the absorber surface and the ambient environment, which enhances radiative heat losses. In addition, the reduced temperature gradient between the absorber wall and the fluid at higher inlet temperatures lowers the driving force for convective heat transfer. Consequently, although higher outlet temperatures can still be achieved, the fraction of absorbed solar energy converted into useful heat decreases with increasing inlet temperature. In this context, the TB design exhibits only a modest reduction in thermal efficiency of about 1% when the inlet temperature increases from 400 K to 550 K, whereas the conventional single-tube receiver experiences a decrease exceeding

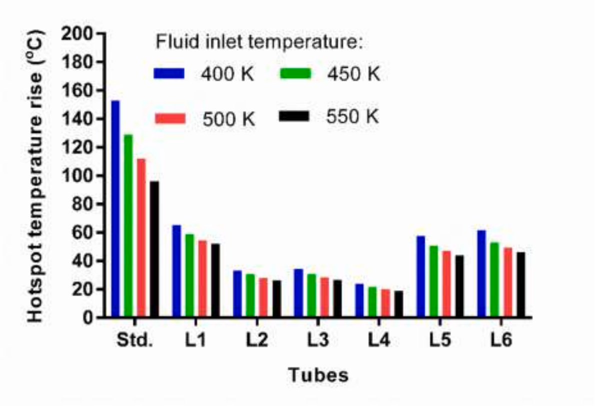

Fig. 19. Maximum tube wall temperature rise obtained at different working conditions.

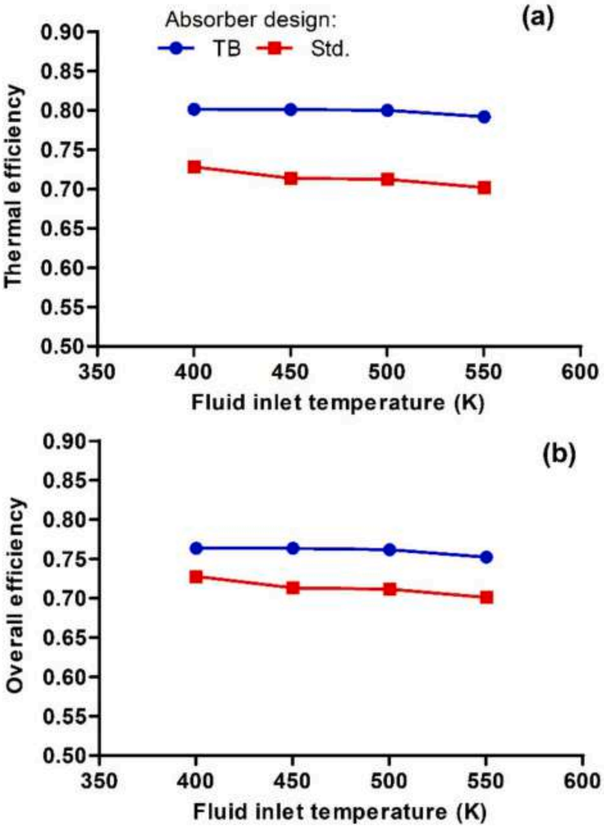

Fig. 20. Performance evaluation for the two receiver designs in terms of (a) thermal and (b) overall efficiency under different fluid inlet temperatures.

3.5% over the same temperature range. These results indicate that the proposed design is more effective in mitigating the increase in thermal losses at elevated operating temperatures. This improved behavior can be attributed to the enhanced heat transfer characteristics of the TB configuration, which result in lower tube wall temperatures and reduced heat losses compared to the standard design.

Taking into account the effects of pressure drop (Fig. 20b), the overall efficiency of the TB configuration remains higher than that of the standard design, confirming the favorable thermo-hydraulic performance of the 12-tube receiver under the investigated operating conditions. Although the influence of the inlet temperature on the overall efficiency is relatively small, the TB design achieves its maximum overall efficiency at an inlet temperature of 450 K, corresponding to an increase of approximately 7% compared to the conventional receiver. These results indicate that the proposed absorber configuration can provide significant performance benefits over a wide range of operating conditions.

5. Conclusions and perspective

This study presents a numerical investigation aimed at assessing the applicability of tube-bundle cavity receivers for PTC systems from a thermo-hydraulic perspective. A three-dimensional CFD model was developed to simulate the operation of the proposed receivers under real-scale operating conditions, based on the specifications of PSA. A two-stage optimization procedure was adopted, considering several alternative designs derived from a prior optical optimization phase. In the first stage, configurations with 6, 12, 18, 24, and 30 tubes were investigated using thermo-hydraulic performance metrics. The results demonstrate that, although the tube-bundle configuration increases flow resistance and pumping power demand, the reduced tube diameter enhances internal fluid velocity and heat transfer between the fluid and the absorber. As a result, the TB design achieves a significant improvement in temperature uniformity, with an increase of up to 23% compared to the standard receiver. By accounting for both thermal gains and hydraulic penalties through the overall efficiency metric, the 12-tube configuration was identified as the most favorable design, reaching a maximum overall efficiency of 0.75. Further analyses of neighboring configurations with 10, 11, 13, and 14 tubes confirmed that the 12-tube layout provides the best performance compromise.

A detailed thermo-hydraulic analysis was subsequently performed on the optimized 12-tube configuration under different fluid inlet temperatures. The main conclusions can be summarized as follows:

- A reverse flow develops inside the outlet manifold, promoting thermal mixing prior to the fluid outlet and significantly reducing the temperature spread at the outlet face compared to the standard design.
- The tube-bundle configuration effectively reduces tube wall temperature non-uniformity. In particular, the L/R1 tube, which experiences the highest thermal load within the cavity, exhibits a temperature rise up to 70% lower than that of the conventional single-tube absorber.
- Increasing the fluid inlet temperature leads to a reduction in thermal efficiency of approximately 3.5% for the conventional receiver, whereas the corresponding reduction for the TB design is limited to about 1%. When accounting for both pressure drop and thermal enhancement, the overall efficiency reaches its maximum at an inlet temperature of 450 K, with an improvement exceeding 7% relative to the conventional design.

These results indicate that the proposed tube-bundle cavity receiver offers a robust thermo-hydraulic performance over a wide range of operating conditions. Nevertheless, the observed efficiency gains must be balanced against additional costs and potential risks associated with increased system complexity. Future work should therefore incorporate complementary analyses, such as thermo-mechanical and economic assessments, to further validate and refine the optimized receiver design prior to practical implementation.

CRediT authorship contribution statement

Hossein Ebadi: Writing – original draft, Visualization, Software, Investigation, Formal analysis, Conceptualization. **Diego-César Alarcón-Padilla:** Writing – review & editing, Validation, Supervision. **Rafael Guedez:** Writing – review & editing, Validation, Supervision, Methodology, Funding acquisition. **Hoda Mahmoudi:** Validation, Supervision, Methodology. **Silvia Trevisan:** Writing – review & editing, Validation, Supervision, Methodology. **Loreto Valenzuela:** Writing – review & editing, Validation, Supervision, Methodology. **Laura Savoldi:** Writing – review & editing, Writing – original draft, Validation, Supervision, Resources, Project administration, Funding acquisition, Conceptualization.

Funding

This research was funded by CETPartnership, the European Partnership under Joint Call 2022 for research proposals, co-funded by the European Commission (GA N°101069750) and with the funding organisations listed on the CETPartnership website. CIEMAT has received funding from the Spanish Ministerio de Ciencia, Innovación y Universidades through the project Ref. PCI2023-146006–2/ MCIU/AEI/https://doi.org/10.13039/501100011033.

Appendix A. . Grid analyses

The sensitivity of the developed grid is presented in terms of changes in pressure drop and fluid outlet temperature rise for all the studied cases. The average cell size in Table A.1 was computed as the $\sqrt[3]{V/N_{\text{cell}}}$ where V is the total volume of the model, and N_{cell} is the cell number. The grid adopted for the simulations is #3, which provides us with numerical results with less than 1% error compared to the finest one (base) in terms of Δp and ΔT_o.

Table A1
Details of the grid convergence results for the all studied cases.

Model	Mesh No.	Average cell size (mm)	$\Delta p/\Delta p_{ref}$	$\Delta T_o/\Delta T_{o,ref}$
Std.	1	5.010	0.870	0.982
	2	3.939	8.900	0.982
	3	2.541	0.990	0.990
	Base	1.563	1	1
6-pipe	1	1.885	0.887	0.878
	2	1.500	0.950	0.902
	3	1.254	0.991	0.991
	Base	1.027	1	1
10-pipe	1	1.090	0.968	0.941
	2	1.051	0.978	0.963
	3	0.969	0.998	0.992
	Base	0.893	1	1
11-pipe	1	1.055	0.964	0.935
	2	0.995	0.971	0.963
	3	0.945	0.999	0.992
	Base	0.917	1	1
12-pipe	1	1.582	0.923	0.913
	2	1.201	0.923	0.957
	3	1.065	0.991	0.993
	Base	0.848	1	1
13-pipe	1	0.979	0.955	0.936
	2	0.946	0.969	0.962
	3	0.894	0.993	0.989
	Base	0.834	1	1
14-pipe	1	0.937	0.967	0.941
	2	0.910	9.744	0.967
	3	0.858	0.999	0.995
	Base	0.803	1	1
18-pipe	1	0.818	0.938	0.918
	2	0.803	0.956	0.954
	3	0.783	0.991	0.991
	Base	0.747	1	1
24-pipe	1	0.703	0.983	0.946
	2	0.699	1.000	0.963
	3	0.672	1.001	0.990
	Base	0.648	1	1
30-pipe	1	0.677	0.978	0.946
	2	0.660	0.983	0.977
	3	0.635	0.990	0.999
	Base	0.614	1	1

Data availability

Data will be made available on request.

References

[1] D. Gielen, F. Boshell, D. Saygin, M.D. Bazilian, N. Wagner, R. Gorini, The role of renewable energy in the global energy transformation, energy, Strateg. Rev. 24 (2019) 38–50, https://doi.org/10.1016/j.esr.2019.01.006.

[2] P. Alamdari, M. Khatamifar, W. Lin, Heat loss analysis review: Parabolic trough and linear Fresnel collectors, Renew. Sustain. Energy Rev. 199 (2024) 114497, https://doi.org/10.1016/j.rser.2024.114497.

[3] Y.-L. He, K. Wang, Y. Qiu, B.-C. Du, Q. Liang, S. Du, Review of the solar flux distribution in concentrated solar power: Non-uniform features, challenges, and

solutions, Appl. Therm. Eng. 149 (2019) 448–474, https://doi.org/10.1016/j.applthermaleng.2018.12.006.

[4] M.I. Khan, R. Gutiérrez-Alvarez, F. Asfand, Y. Bicer, S. Sgouridis, S.G. Al-Ghamdi, H. Jouhara, M. Asif, T.A. Kurniawan, M. Abid, A. Pesyridis, M. Farooq, The economics of concentrating solar power (CSP): Assessing cost competitiveness and deployment potential, Renew. Sustain. Energy Rev. 200 (2024) 114551, https://doi.org/10.1016/j.rser.2024.114551.

[5] M.T. Islam, N. Huda, A.B. Abdullah, R. Saidur, A comprehensive review of state-of-the-art concentrating solar power (CSP) technologies: current status and research trends, Renew. Sustain. Energy Rev. 91 (2018) 987–1018, https://doi.org/10.1016/j.rser.2018.04.097.

[6] A. Kasaeian, A. Kouravand, M.A. Vaziri Rad, S. Maniee, F. Pourfayaz, Cavity receivers in solar dish collectors: a geometric overview, Renew. Energy 169 (2021) 53–79, https://doi.org/10.1016/j.renene.2020.12.106.

[7] S. Rodat, R. Thonig, Status of Concentrated Solar Power Plants Installed Worldwide: past and present Data, Clean Technol. 6 (2024) 365–378, https://doi.org/10.3390/cleantechnol6010018.

[8] M. Shahzad Nazir, A. Shahsavar, M. Afrand, M. Arıcı, S. Nižetić, Z. Ma, H.F. Öztop, A comprehensive review of parabolic trough solar collectors equipped with turbulators and numerical evaluation of hydrothermal performance of a novel model, Sustain. Energy Technol. Assessments. 45 (2021), https://doi.org/10.1016/j.seta.2021.101103.

[9] Z.A. Nawsud, A. Altouni, H.S. Akhijahani, H. Kargarsharifabad, A comprehensive review on the use of nano-fluids and nano-PCM in parabolic trough solar collectors (PTC), Sustain. Energy Technol. Assessments. 51 (2022) 101889, https://doi.org/10.1016/j.seta.2021.101889.

[10] E. Bellos, C. Tzivanidis, Alternative designs of parabolic trough solar collectors, Prog. Energy Combust. Sci. 71 (2019) 81–117, https://doi.org/10.1016/j.pecs.2018.11.001.

[11] K. B., M.A. Hassan, A.K. Pandey, S. Chinnasamy, Linear cavity solar receivers: A review, Appl. Therm. Eng. 221 (2023) 119815. https://doi.org/10.1016/j.applthermaleng.2022.119815.

[12] Y. Cengel, A. Ghajar, Heat and mass transfer: fundamentals and applications, 2015.

[13] F. Cao, L. Wang, T. Zhu, Design and Optimization of Elliptical Cavity Tube Receivers in the Parabolic Trough Solar Collector, Int. J. Photoenergy 2017 (2017) 1471594, https://doi.org/10.1155/2017/1471594.

[14] X. Li, H. Chang, C. Duan, Y. Zheng, S. Shu, Thermal performance analysis of a novel linear cavity receiver for parabolic trough solar collectors, Appl. Energy 237 (2019) 431–439, https://doi.org/10.1016/j.apenergy.2019.01.014.

[15] D.A. Boyd, R. Gajewski, R. Swift, A cylindrical blackbody solar energy receiver, Sol. Energy. 18 (1976) 395–401. https://doi.org/https://doi.org/10.1016/0038-092X(76)90004-9.

[16] O.A. Barra, L. Franceschi, The parabolic trough plants using black body receivers: Experimental and theoretical analyses, Sol. Energy 28 (1982) 163–171, https://doi.org/10.1016/0038-092X(82)90295-X.

[17] R. Bader, A. Pedretti, M. Barbato, A. Steinfeld, An air-based corrugated cavity-receiver for solar parabolic trough concentrators, Appl. Energy 138 (2015) 337–345, https://doi.org/10.1016/j.apenergy.2014.10.050.

[18] H. Liang, C. Zhu, M. Fan, S. You, H. Zhang, J. Xia, Study on the thermal performance of a novel cavity receiver for parabolic trough solar collectors, Appl. Energy 222 (2018) 790–798, https://doi.org/10.1016/j.apenergy.2018.04.030.

[19] M. Sharifzadeh, R. Loni, Performance of a solar parabolic trough concentrator using vacuum linear V-shaped cavity receiver, Therm. Sci. Eng. Prog. 51 (2024) 102609, https://doi.org/10.1016/j.tsep.2024.102609.

[20] R. Loni, M. Sharifzadeh, Performance comparison of a solar parabolic trough concentrator using different shapes of linear cavity receiver, Case Stud. Therm. Eng. 60 (2024) 104603, https://doi.org/10.1016/j.csite.2024.104603.

[21] R. Loni, B. Ghobadian, A.B. Kasaeian, M.M. Akhlaghi, E. Bellos, G. Najafi, Sensitivity analysis of parabolic trough concentrator using rectangular cavity receiver, Appl. Therm. Eng. 169 (2020) 114948, https://doi.org/10.1016/j.applthermaleng.2020.114948.

[22] X. Xiao, P. Zhang, D.D. Shao, M. Li, Experimental and numerical heat transfer analysis of a V-cavity absorber for linear parabolic trough solar collector, Energy Convers. Manag. 86 (2014) 49–59, https://doi.org/10.1016/j.enconman.2014.05.001.

[23] F. Chen, M. Li, P. Zhang, X. Luo, Thermal performance of a novel linear cavity absorber for parabolic trough solar concentrator, Energy Convers. Manag. 90 (2015) 292–299, https://doi.org/10.1016/j.enconman.2014.11.034.

[24] H. Ebadi, S. Kamfiroozi, A. Cammi, L. Savoldi, Optical Performance of a Novel Tube-Bundle Cavity Receiver for Solar Parabolic Trough Collectors (2022), https://doi.org/10.1115/POWER2022-85631.

[25] H. Ebadi, D.-C. Alarcón-Padilla, J.J. Contreras Keegan, R.E. Guedez Mata, S. Trevisan, L. Valenzuela Gutiérrez, E. Zarza Moya, L. Savoldi, Optical Analysis and Optimization of a New Receiver for Solar Parabolic Trough Collectors (DETECTIVE), (2024). https://doi.org/10.1115/ES2024-130019.

[26] L. Valenzuela, R. López-Martín, E. Zarza, Optical and thermal performance of large-size parabolic-trough solar collectors from outdoor experiments: a test method and a case study, Energy 70 (2014) 456–464, https://doi.org/10.1016/j.energy.2014.04.016.

[27] W.C. Swinbank, Long-wave radiation from clear skies, Q. J. R. Meteorol. Soc. 89 (1963) 339–348, https://doi.org/10.1002/qj.49708938105.

[28] E. Bellos, I. Daniil, C. Tzivanidis, Multiple cylindrical inserts for parabolic trough solar collector, Appl. Therm. Eng. 143 (2018) 80–89, https://doi.org/10.1016/j.applthermaleng.2018.07.086.

[29] M. Wirz, J. Petit, A. Haselbacher, A. Steinfeld, Potential improvements in the optical and thermal efficiencies of parabolic trough concentrators, Sol. Energy 107 (2014) 398–414, https://doi.org/10.1016/j.solener.2014.05.002.

[30] M.A. Alzoubi, A.P. Sasmito, Thermal performance optimization of a bayonet tube heat exchanger, Appl. Therm. Eng. 111 (2017) 232–247, https://doi.org/10.1016/j.applthermaleng.2016.09.052.

[31] B.S. Petukhov, Heat Transfer and Friction in Turbulent Pipe Flow with Variable Physical Properties, in: J.P. Hartnett, T.F.B.T.-A. in H.T. Irvine (Eds.), Elsevier, 1970: pp. 503–564. https://doi.org/10.1016/S0065-2717(08)70153-9.

[32] W. Al-Aloosi, Y. Alaiwi, H. Hamzah, Thermal performance analysis in a parabolic trough solar collector with a novel design of inserted fins, Case Stud. Therm. Eng. 49 (2023) 103378, https://doi.org/10.1016/j.csite.2023.103378.

[33] Y. Han, L. Li, S. Wang, Z. Bai, Q. Li, A coupled optical-thermal-fluid-structural analysis of parabolic trough solar collector by deformation coupling instant ray-tracing multiple iteration method, Sol. Energy Mater. Sol. Cells 279 (2025) 113221, https://doi.org/10.1016/j.solmat.2024.113221.